

Ru(II)-NO Complexes of Pyrone-Based Sulfa Drug Schiff Bases: Synthesis, DFT and *In silico* ADME a Theoretical Approach

Pradeep Kumar Vishwakarma ^{1,*} , Pushpendra Singh Jaget ¹, Mahendra Kumar Parte ¹, Deepak Kumar Rajak ¹, Ram Charitra Maurya ¹ , Sutapa Roy ²

¹ Department of Chemistry and Pharmacy, Rani Durgavati Vishwavidyalaya, Jabalpur (M.P.) India

² Department of Chemistry, St Aloysius College, Jabalpur (M.P.) India

* Correspondence: pkvchemrduni1@gmail.com (P.K.V.);

Scopus Author ID:18438745100

Received: 24.01.2024; Accepted: 30.06.2024; Published: 15.02.2025

Abstract: Synthesis of two ruthenium(II)nitrosyl complexes, formed by the interaction of $[\text{RuCl}_3(\text{NO})(\text{PPh}_3)_2]$ with monobasic bidentate Schiff base ligands [**HL**¹: *N*-(3-Acetyl-2-hydroxy-6-methyl-4H-pyran-4-one)-sulfanilamide and **HL**²: *N*-(3-Acetyl-2-hydroxy-6-methyl-4H-pyran-4-one)-sulfaguanidine] in aqueous ethanol is described. The resulting two mononuclear Ruthenium(II)-NO complexes, namely, *cis*- $[\text{RuCl}_2(\text{NO})(\text{PPh}_3)(\text{L}^1)]$ **C1** and *cis*- $[\text{RuCl}_2(\text{NO})(\text{PPh}_3)(\text{L}^2)]$ **C2** were characterized through various spectral (FTIR, ¹H-NMR and UV/Vis.) and physicochemical techniques. Electrochemistry was studied using the cyclic voltammetric technique. Then, the Gaussian 09 program was used for optimized molecular structure, electronic surface analysis, and NLO properties through DFT approaches via a mixed basis set at the B3LYP/LANL2DZ level of theory. The ¹H-NMR spectra of the compounds were computed by the GIAO method and correlated to the experimental chemical shift. The TD-DFT-based electronic absorption spectra were computed using the PCM model. Furthermore, the in-vitro antioxidant activity of the studied compounds was monitored via two radical scavenging inhibitors, and the antibacterial activity was investigated against strains of *E. coli*. Finally, the synthesized compounds predicted their *in silico* ADME properties, showing good physicochemical and bioactivity.

Keywords: Ru(II)-NO; MEP; NLO; antioxidant; ADME.

© 2025 by the authors. This article is an open-access article distributed under the terms and conditions of the Creative Commons Attribution (CC BY) license (<https://creativecommons.org/licenses/by/4.0/>).

1. Introduction

The ruthenium nitrosyl complexes are the most effective inorganic NO carriers and can be used for precise NO delivery to cells with photochemical activation [1-3]. Interest in ruthenium nitrosyl complexes is highly determined by their potential as NO-releasing substances. Nitric oxide plays an essential role in blood pressure control and nitrosative and oxidative stress mechanisms [4-8]. Thus, various ruthenium compounds have been explored as NO carriers with photochemical or reductive control of NO release [9-13]. Specific photoinduced NO toxicity [14] allows for possible use in PDT applications. In addition, the fundamental interest in nitrosyl complexes is determined by their redox, electronic properties, and Ru-NO/Ru-ON isomerization [15-22]. Various TM nitrosyl complexes have been investigated as potential carriers able to deliver NO on-demand in biological tissues upon illumination, such as photodynamic therapy (PDT) to treat cancers [22]. Ruthenium-based

complexes show great promise because of their lower toxicity compared to some other metals, different mechanisms of action, a different preference for protein rather than DNA binding compared to platinum drugs, and a diverse spectrum of activity without pronounced cross-resistance [23]. The biological activity of nitrosyl ruthenium complexes is associated with the participation of free (NO) and coordinated (NO⁺) molecules in the physiological processes [24]. The complexes have been reported as the influential donors of NO [25]. Ruthenium(II) nitrosyl complexes have the ability to release NO while exposing low-energy radiation [26]. Antimicrobial, antiviral, and anticancer disease treatment could potentially be addressed using many of these metal-Schiff base derivatives as potential drugs [27].

Most of the reports on molecular modeling and theoretical studies based on DFT have been reported in recent years. In connection with this, the objective of the present work summarizes the theoretical cum experimental investigations of Schiff base based on N-dehydroacetic acid-sulfanilamide or sulfaguanidine and their Ru(II) nitrosyl complexes formulated as *cis*-[RuCl₂(NO)(PPh₃)(L_{1,2})]. The characterization of both the synthesized compounds was done using physicochemical and spectral techniques, and they also had a correlation with computed spectral assignments. The current work involves the study of the target compound's molecular structure, charge analysis, FMOs, molecular docking, and antioxidant aspects. The *in silico* ADME results are attributed to good pharmacokinetics and biological activity.

2. Material and Method

All chemicals are analytical grade and used without further purification. The electronic absorption spectra were recorded on Carry 5000 UV-Vis/NIR spectrophotometer. The solid-state FT-IR spectra were observed with an α T Bruker FT-IR spectrophotometer from 4000-500 cm⁻¹ using the KBr pellet technique. The electrochemical studies were performed on the Epsilon (BASi Cell Stand) system. ¹H-NMR spectra of compounds **C1** and **C2** were obtained from CDRI, Lucknow. The molar conductance of complexes in DMF solution (10⁻³) at room temperature was recorded using the EUTECH model CON2700 direct digital reading conductivity meter. The molar conductivity of the title complex is 12.47 and 12.36 Ω⁻¹ cm² mol⁻¹.

2.1. Antioxidant activity.

Two assays were used to measure the antioxidant activity: the free radical-scavenging (FRS) activity of the title complexes was measured using the Li *et al.* method. [28]. Through this procedure, 2 ml of a 4 % solution of DPPH radical in methanol (w/v) was mixed with 500 µl of sample solutions at various concentrations (20, 40, 60, 80, and 100 µM). From electronic spectra, the absorbance at 517 nm was measured after a half-hour of incubation of the reaction within the dark compared with the absorbance of control prepared similarly without the addition of the compound. The absorbance was decreased with increasing concentration. The minor absorbance indicates the reaction mixture's better free radical scavenging activity.

Nitric oxide radical (NOR) scavenging activity of the studied complex compounds was measured through a slightly modified procedure [29,30]. Both compounds were dissolving in DMF at different concentrations (20, 40, 60, 80, and 100 µM), and homogeneous solutions were obtained by stirring. Nitric oxide radicals (NOR) were generated from 1mL of sodium

nitroprusside (10 mM), and 1.5 mL of phosphate buffer saline (0.2 M, pH 7.4) were added to the test compounds and incubated for 150 min at 25°C. The reaction mixture of the above samples (1 mL each) was treated with 1 mL of Griess reagent (1% sulfanilamide, 2% H₃PO₄, and 0.1% naphthalene diamine dihydrochloride). Butylated hydroxytoluene (BHT) was used as a positive control. The absorbance was measured at 546 nm.

In the two assays described above, all the tests were course in triplicate, and various concentrations of the complexes were used to fix a concentration at which the compound showed around 50% scavenging activity. In addition, the percentage of scavenging activity was calculated via the given formula:

$$\text{Percentage of scavenging activity} = [(A_0 - A_C) / A_0] \times 100 \quad (1)$$

A₀ and A_C are the absorbances in the absence and presence of the complex, respectively). Thus, 50% of scavenging activity (IC₅₀) can be calculated using the percentage of scavenging activity results.

2.2. Computational details.

Computational calculations of the studied compounds **C1** and **C2** were done via the Gaussian 09 application package [31] using B3LYP/LAN2DZ basis sets. The molecular optimization of the compounds produced no imaginary wavenumbers on the calculated vibrational spectrum, confirming that the shape assumed corresponds to minimal energy. The computed wavenumbers and their assignments are aided by using the animation choice of the GAUSSVIEW 5.0 application, which visually presents the vibrational modes [32]. UV-visible spectra had been computed through the TD-DFT approach [33]. The electronic absorption spectra of the compounds with the usage of the DMSO solvent Polarizable Continuum Model (PCM). In addition, ¹H-NMR spectra were calculated using the GIAO method, and TMS was used as reference material in the calculation of the chemical shift values.

2.3. Synthesis of Schiff base ligands.

Sulfa drug-derived Schiff base ligands were prepared by refluxing with constant stirring of dehydroacetic acid (840 mg, 5 mmol) with sulfanilamide (860 mg, 5 mmol) or sulfaguanidine (1070 mg, 5 mmol) in 1:1 molar ratio, 6 hrs in 20 ml ethanol. Then, the desired compounds were precipitated and filtered off, washed with ethanol, recrystallized from ethanol, and dried in CaCl₂.

HL1: Anal. Calcd. for C₁₄H₁₄N₂O₅S: C, 52.17; H, 4.38; N, 8.69. Found: C, 52.25; H, 4.00; N, 8.85 %. Yield: 1.230 g, 72%. Color: Cream and decomposition temperature 195°C. IR (KBr, cm⁻¹): experimental [theoretical] in gaseous mode: ν(O-H); 3422 [3631], ν(C-H) aromatic; 3220 [3209] ν(C-H) aliphatic; 2925 [3046], ν(C=O) lactone; 1685 [1696], ν(C=N); 1570 [1622], ν(C-O); 1340 [1388] and ν(N-N); 1005 [1076], ν(O=S=O) asymmetric 1265 [1233], and ν(O=S=O) symmetric 1167 [1127] cm⁻¹.

HL2: Anal. Calcd. for C₁₅H₁₆N₄O₅S: C, 49.44; H, 4.43; N, 15.38, Found: C, 48.98; H, 4.55; N, 15.15 %. Yield: 1.440 g, 75%. Color: White and decomposition temperature 190°C. IR (KBr, cm⁻¹): experimental [theoretical] in gaseous mode: ν(O-H); 3424 [3639], ν(N-H); 3301 [3513], ν(C-H) aromatic; 3222 [3350] ν(C-H) aliphatic; 2925 [3295], ν(C=O) lactone; 1699 [1711], ν(C=N); 1572 [1657], ν(C-O); 1385 [1360] and ν(N-N); 1056 [1068], ν(O=S=O) asymmetric 1264 [1268], and ν(O=S=O) symmetric 1164 [1128] cm⁻¹.

2.4. Synthesis of complexes C1 and C2.

Ru(II) nitrosyl complexes **C1** and **C2** were prepared by refluxing with constant stirring of $\text{RuCl}_3\text{NO}(\text{PPh}_3)_2$ (381 mg, 0.5 mmol) with N-dehydroacetic acid-sulfanilamide (HL1, 160 mg, 0.5 mmol), N-dehydroacetic acid-sulfaguanidine (HL2, 180 mg, 0.5 mmol), respectively in 1:1 molar ratio, 6 hrs in 20ml ethanol. Then, the desired compounds were precipitated and filtered off, washed with ethanol, and recrystallized from ethanol. Anal. Calcd. for $\text{cis-}[\text{RuCl}_2(\text{NO})(\text{PPh}_3)(\text{L}_1)]$ **C1**, $\text{C}_{32}\text{H}_{28}\text{Cl}_2\text{N}_3\text{O}_6\text{PRuS}$: C, 48.92; H, 3.59; N, 5.35. Found: C, 48.89; H, 3.55; N, 5.29 %. Yield: .416 g, 64%. Colour: Cream and decomposition temperature 240°C . IR (KBr, cm^{-1}): experimental [theoretical] in gaseous mode: $\nu(\text{O-H})$; 3433 [not found], $\nu(\text{N-H})$; 3310 [3504], $\nu(\text{C-H})$ aromatic; 3071 [3228] $\nu(\text{C-H})$ aliphatic; 2926 [3056], $\nu(\text{C=O})$ lactone; 1734 [17046], $\nu(\text{C=N})$; 1633 [1569], $\nu(\text{C-O})$; 1322 [1376] and $\nu(\text{N-N})$; 1091 [986], $\nu(\text{O=S=O})$ asymmetric 1236 [1263], and $\nu(\text{O=S=O})$ symmetric 1168 [1177] cm^{-1} .

Anal. Calcd. For $\text{cis-}[\text{RuCl}_2(\text{NO})(\text{PPh}_3)(\text{L}_2)]$ **C2** $\text{C}_{33}\text{H}_{30}\text{Cl}_2\text{N}_5\text{O}_6\text{PRuS}$: C, 47.89; H, 3.65; N, 8.46, Found: C, 48.15; H, 3.55; N, 08.29 %. Yield: 464 g, 69%. Color: Light brown and decomposition temperature 230°C . IR (KBr, cm^{-1}): experimental [theoretical] in gaseous mode: $\nu(\text{O-H})$; 3432 [not found], $\nu(\text{N-H})$; 3211 [3395], $\nu(\text{C-H})$ aromatic; 3071 [3230] $\nu(\text{C-H})$ aliphatic; 2927 [3055], $\nu(\text{C=O})$ lactone; 1699 [1711], $\nu(\text{C=N})$; 1635 [1652], $\nu(\text{C-O})$; 1322 [1379] and $\nu(\text{N-N})$; 1057 [985], $\nu(\text{O=S=O})$ asymmetric 1273 [1236], and $\nu(\text{O=S=O})$ symmetric 1153 [1182] cm^{-1} .

3. Result and Discussions

Sulfa drug-derived Schiff base ligands $\text{HL}^{1,2}$ and its ruthenium(II) nitrosyl complexes $\text{cis-}[\text{Ru}(\text{Cl})_2(\text{NO})(\text{PPh}_3)(\text{L}^1)]$ **C1** and $\text{cis-}[\text{Ru}(\text{Cl})_2(\text{NO})(\text{PPh}_3)(\text{L}^2)]$ **C2** were synthesized from the following synthetic route shown in Figure 1. The proposed conformation and composition have been confirmed by various analytical techniques. The ligands and complexes' decomposition temperatures were also recorded; the ligand showed a value around $195\text{-}200^\circ\text{C}$ after the complexation increased around $230\text{-}260^\circ\text{C}$, giving clear information about metal-ligand binding.

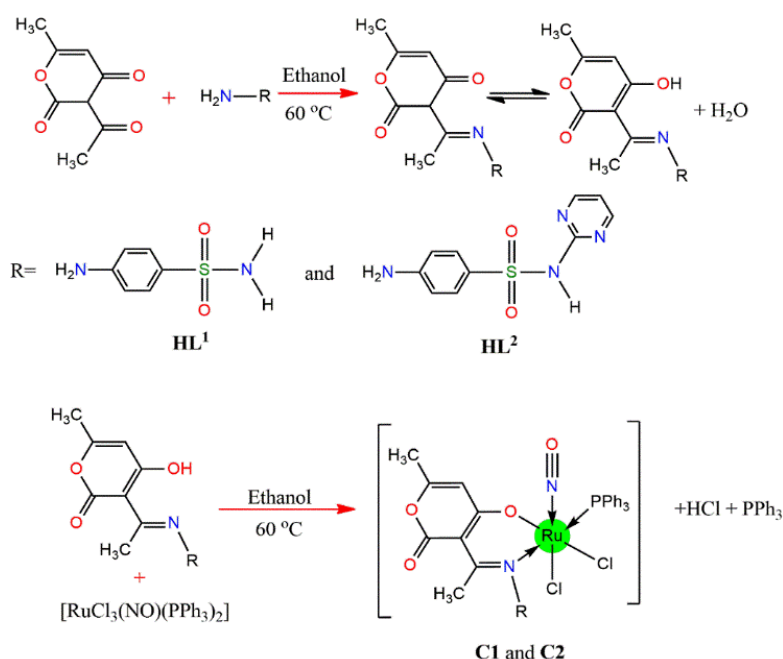


Figure 1. Synthetic route of ligands and $\text{cis-}[\text{RuCl}_2(\text{NO})(\text{PPh}_3)(\text{L}^{1,2})]$ **C1** and **C2** complexes.

3.1. Spectral studies.

Figures 2 and Supplementary Figure 1 depicted the vibrational spectra of the sulfa drug-based ligands. In all ligands, the three characteristic stretching vibrations bands are observed as $[3422-3427, \nu(\text{OH})]$; $[3220-3222, \nu(\text{NH})]$ and $[1633-1643, \nu(\text{C}=\text{N})]$ cm^{-1} . After the complexation, the spectral band of $[\nu(\text{C}=\text{N}) \sim 1633 \text{ cm}^{-1}]$ is shifted in inferior frequency at $\sim 1603 \text{ cm}^{-1}$. The band at $\sim 3425 \text{ cm}^{-1}$ $\nu(\text{OH})$ does not appear in the complexes, confirming the metal-ligand bonding. At the same time, the new strong band is arising at $\sim 3400 \text{ cm}^{-1}$ of the lattice water or moisture of the molecule. The symmetric and asymmetric stretching frequencies of $\nu(\text{O}=\text{S}=\text{O})$ in the ligands and complexes were attributed at ~ 1180 and $\sim 1260 \text{ cm}^{-1}$. In the infrared spectra of complex molecules, one characteristic peak appeared at 1870 cm^{-1} , representing that they were true of the $[\text{Ru}^{\text{II}}-\text{NO}^+]$ nature [34]. The nitrosyl complexes, namely, **C1** and **C2** in this work, display the band for $\nu(\text{NO})$ in the spectrums at 1873 and 1872 cm^{-1} , respectively. The coordinated terminal nitrosyl is detected in a slightly higher zone than the precursor complexes. They are close to the theoretical frequency of all respective complex molecules. The other remaining spectral peaks at 448 to 996 cm^{-1} designate the coordination core of the complex. The experimental and theoretical infrared spectra of *cis*- $[\text{Ru}^{\text{II}}\text{Cl}_2(\text{NO})(\text{L}^1)_2](\text{PPh}_3)$ **C1** and **C2** are displayed in Figures 3 and S2. The correlation, along with the experimental/theoretical vibrational frequencies, was monitored as linear and characterized by the equations in $[y=1.0591x-76543(\text{R}^2=0.9955)]$ and $[y=1.0975x-158.78(\text{R}^2=0.9953)]$ for selective compounds HL^1 and **C1**, respectively Figures S3 and 4. Some slight variations are observed in experimental and theoretical frequencies, which are affected by some of the experimental condition's polarization and computation effects.

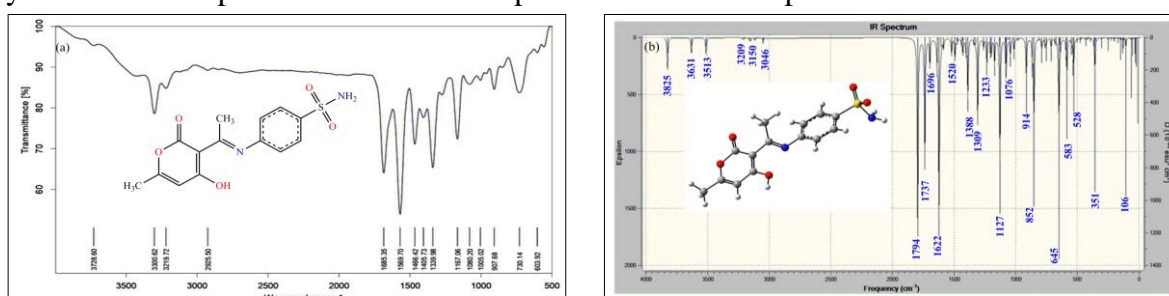


Figure 2. (a) Experimental; (b) theoretical IR spectrum of HL^1 .

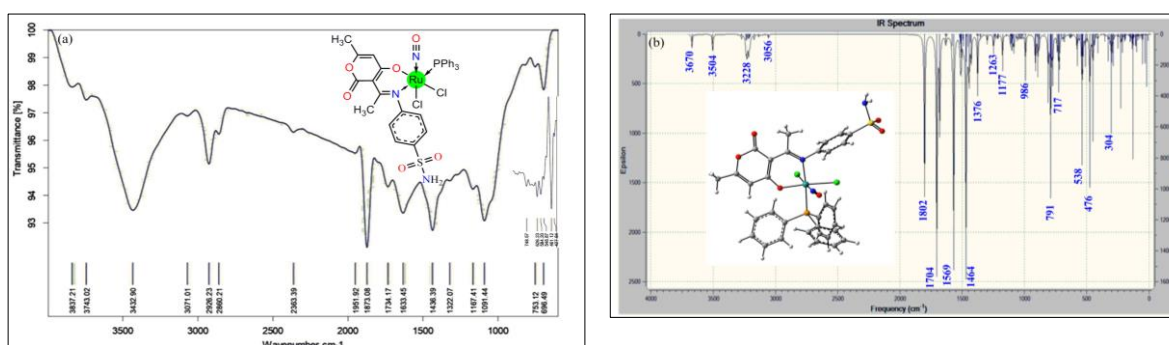


Figure 3. IR spectrum of *cis*- $[\text{RuCl}_2(\text{NO})(\text{PPh}_3)(\text{L}^1)]$ **C1** (a) experimental; (b) theoretical.

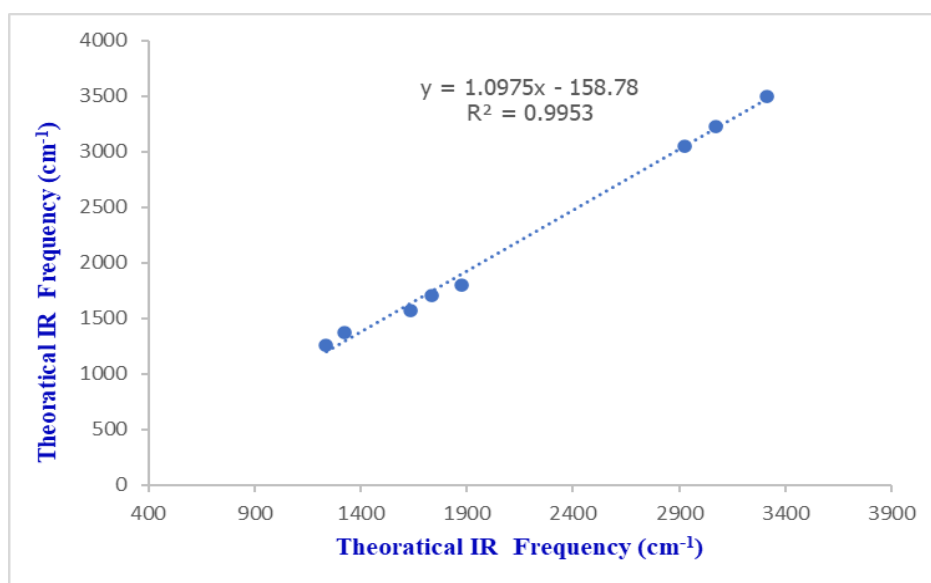


Figure 4. The relationship graphs between the experimental and theoretical vibrational frequency of C1.

Figure 5 depicts the electronic spectra of **C1** and **C2**. The spectra were recorded in a DMSO (10-4 M) solution. In comparison, then the theoretical electronic spectra were computed by the PCM model system using the TD-DFT method. The experimental/theoretical instance band at ~276/335 nm for all the studied compounds is most likely the $\pi \rightarrow \pi^*$ (sulfa drugs) intra-ligand charge transfer transitions. The band at ~317/395 nm is possibly LMCT, and finally, the band at ~402/410 nm is probably MLCT bands ($d\pi(\text{Ru}) \rightarrow \pi^*(\text{NO})$). The transitions from HOMO-1 \rightarrow LUMO, HOMO \rightarrow LUMO+1, and HOMO \rightarrow LUMO at ~331, ~393, and ~403 nm, respectively, resulted from mixing excitations configurations having significant coefficients in CI wave function. DFT and TDDFT calculations have shown that the photoactive bands are organized primarily through ligand-to-ligand charge transfer (LLCT) of $\pi(\text{L}) \rightarrow \pi^*(\text{Ru}-\text{NO})$, suggesting that the LLCT was responsible for initiating the NO photo release. By using femtosecond (fs) time-resolved mid-IR spectroscopy, we investigated how NO is released from complexes in DMSO during 331 nm excitation [35]. The diagrams of the participating FMOs are given in Figure S4, and data are charted in Table 1. The observation clearly shows the coordinated organic framework, and the minor upsurge absorption near-visible region indicates the nitrosyl ligand's photo lability [36]. The conversation looks prolific in HOMO (depopulating) and LUMO (populating) to carry out the bonding and antibonding of Ru-NO, respectively, for generating the NO release. The orbital numbers 165 and 176 are destined for HOMO, while 177 and 166 are for LUMO of **C1** and **C2**, respectively. The observation may indicate the photoinduced release of NO from the complexes.

Table 1. Electronic absorption and TD-DFT for the complexes C1 and C2 here [OS= oscillator strength, major orbital contribution= MOC].

Comp.	Wavelength (nm)		eV.	OS (<i>f</i>) <i>f</i> osc ($\times 10^{-4}$)	MOC (%)	Transitions Assignment
	Exp.	Comp.				
C1	273	333	3.723	6.14	H-1(α) \rightarrow L(α)(41)	ILCT
	317	395	3.139	2.08	H(α) \rightarrow L+1(α)(61)	LMCT
	405	402	3.084	1.03	H(α) \rightarrow L(α) (62)	MLCT
C2	274	319	3.887	9.45	H-1(α) \rightarrow L+1(α)(34)	ILCT
	318	410	3.024	6.18	H(α) \rightarrow L(α) (48)	LMCT
	408	419	2.959	2.09	H(α) \rightarrow L+1(α)(51)	MLCT

Table 2. The HOMO-LUMO values from electrochemical and electronic absorption spectroscopic data.

Comp.	E_{ox} V (From CV)	E_{HOMO} eV [$E_{ox}-E_{1/2}+4.8$]	Optical band gap from absorption studies (eV) $1242/\lambda(\text{nm})$	E_{LUMO} (E_{HOMO} -optical band gap)	E_{HOMO} - LUMO	E_{HOMO} -LUMO (TD-DFT)
C1	-0.223	4.27	4.55	-0.28	4.55	2.99
C2	-0.190	4.31	4.53	-0.22	4.31	2.94

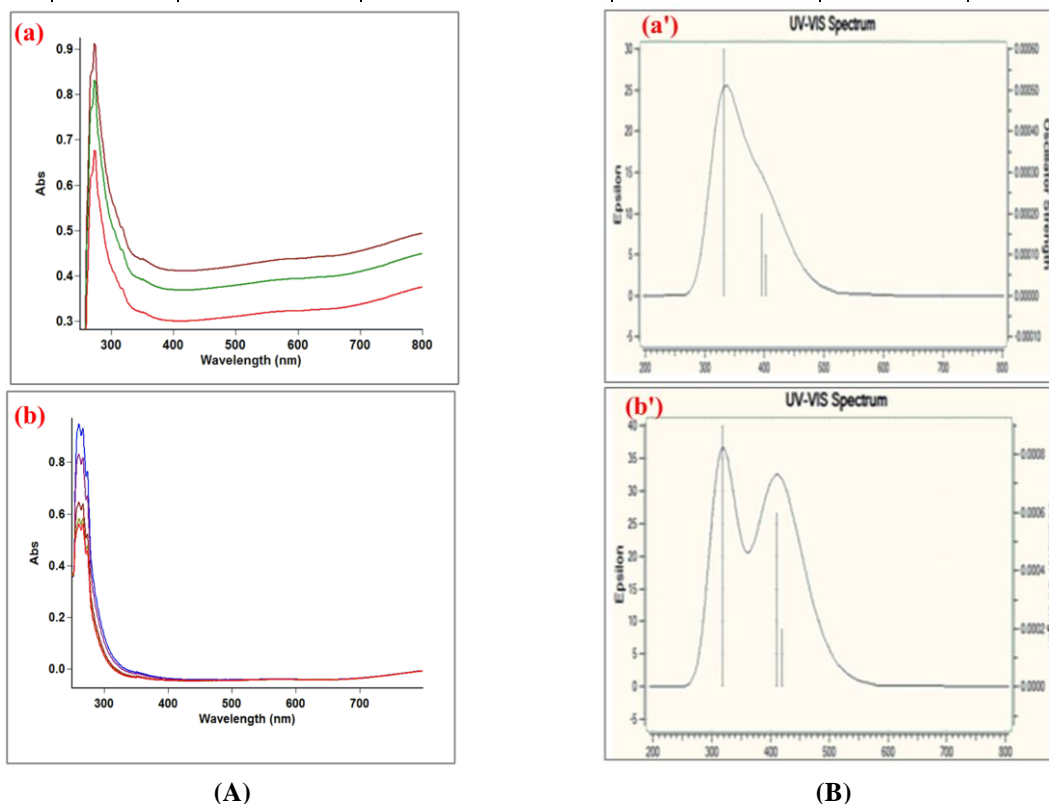
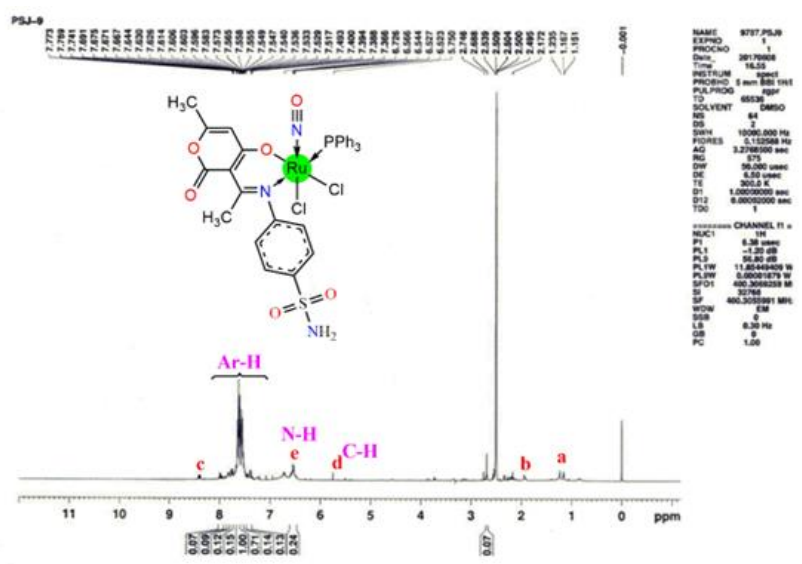
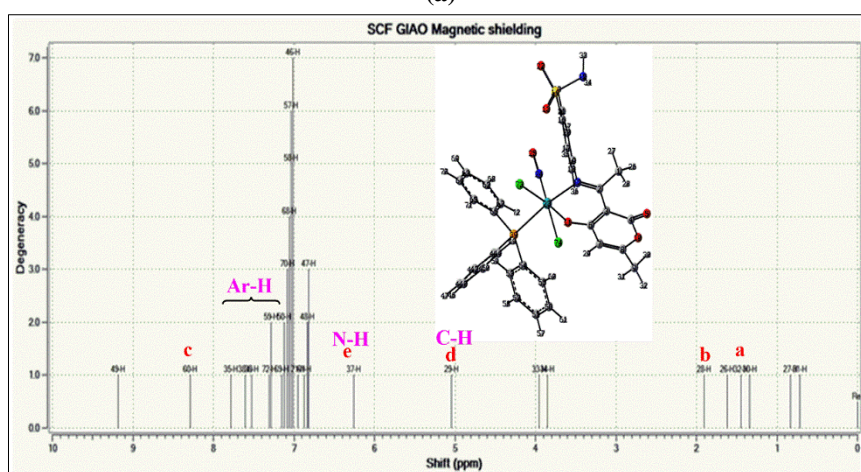


Figure 5. (A) Experimental; (B) theoretical UV-vis spectra of **C1** and **C2**.

The experimental cum theoretical $^1\text{H-NMR}$ spectrum of both studied complexes **C1** and **C2** is displayed in Figures 6 and S5. The experimental $^1\text{H-NMR}$ spectra were recorded at RT using a DMSO- d_6 . While the theoretical $^1\text{H-NMR}$ spectral studies were done with the GIAO approach, TMS was used as reference material to the DFT approach. The theoretical ^1H -chemical shifts $\delta(\text{ppm})$ data is given in parenthesis. The singlet peak found at ~ 5.7 (4.9, 5.1, and 5.3) ppm is attributed to the proton of the lactone ring of the dehydroacetic part in all the studied compounds. A peak was found at ~ 6.5 (6.3, 6.4, and 6.2) in ppm corresponding to the -NH of the sulfa drug part of the Schiff base ligands. Multiple peaks were observed in the region 7.0-7.9 (6.7-7.5) δ ppm is assigned as aromatic ring protons. The singlet signals have been observed due to three protons at [~ 1.3 (1.4) ppm, $\text{CH}_3\text{-C(a)}$] and [~ 1.9 (1.8) ppm, $\text{CH}_3\text{-C=N(b)}$] for the three protons. The singlet peak was observed at 8.4 (8.2) δ ppm due to a single proton of H-C=N(c) . The septet peak arrival of five singlets around 2.5 ppm can be assigned to the presence of solvent (DMSO), which does not appear in the theoretical spectrum. The graphical presentation demonstrates a notable resemblance between the experimental and theoretical findings, which validate the applied computational approaches. The comparison was expressively in agreement, and the correlation graphs are displayed in Figure 7. The experimental and theoretical chemical shifts of the representative compound **C1** were linear and characterized by the equations of [$y=0.9493x-0.0001$ ($R^2=0.9914$)]. Some slight variations are observed in experimental and theoretical chemical shifts, which are affected by some of the experimental condition's polarization and computation effects.



(a)



(b)

Figure 6. (a) Experimental; (b) theoretical ¹H-NMR spectrum of *cis*-[RuCl₂(NO)(PPh₃)(L¹)] **C1**.

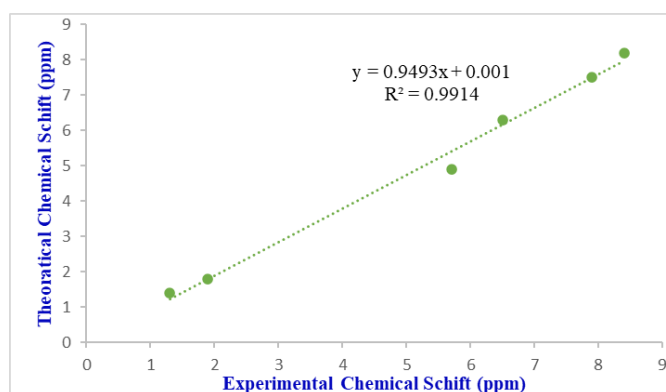
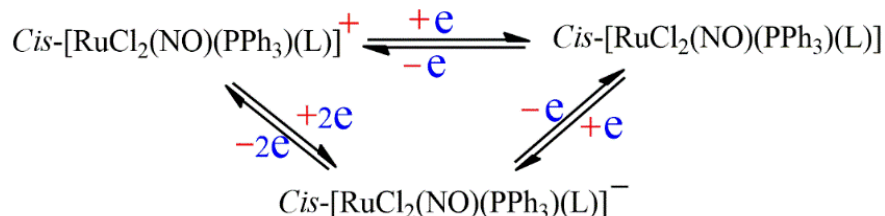


Figure 7. The relationship graphs between the experimental and theoretical chemical shift of **C1**.

3.2. Electrochemistry.

The electrochemical properties of the studied complexes **C1** and **C2** were monitored in the potential range between ± 1.500 V v/s Ag/AgCl in a 0.1M solution of TBAP as a supporting electrolyte. Figure 8 depicts the compounds' voltammogram at four variable scan ranges (100, 200, 300, and 400 mV/Sc). They were characterized by two irreversible waves centered at the coordinated NO⁺ ligand [37]. The voltammogram of compounds **C1** and **C2** shows two-electron two-step irreversible reduction waves as [E_{pc1}(0.179), (0.168), (0.156) and E_{pc2}(-

0.581), (-0.639), (-0.557)V], and [I_{pc1} (-0.893), (-0.353), (-0.872) and I_{pc2} (-2.752), (-3.624), (-2.052) μ A] that can be used to establish $Ru-NO^+ \rightarrow Ru-NO^0$ and $Ru-NO^0 \rightarrow Ru-NO^-$ components. And two electrons in single-step irreversible oxidation wave as [E_{pa} (-0.223), (-0.190), (-0.237) V] and [I_{pc} (0.583), (0.959), (0.307) μ A] that can be used to establish $Ru-NO^- \rightarrow Ru-NO^0$ and $Ru-NO^0 \rightarrow Ru-NO^+$ components, the complexes undergo two redox process described in Scheme 3.



Scheme 3. $Ru-NO^- \rightarrow Ru-NO^0$ and $Ru-NO^0 \rightarrow Ru-NO^+$ components, the complexes undergo two redox process.

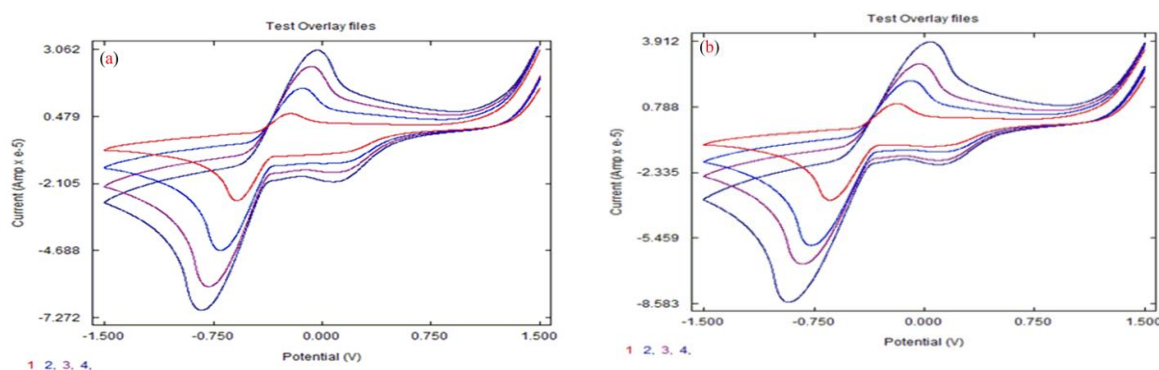


Figure 8. CV for synthesized Ru(II)-nitrosyl compounds and (a) **C1**; (b) **C2**.

Such electron movement analysis may be associated with FMOs studies that significantly influence the formulation of chemical descriptors [38]. The HOMO, LUMO, and their energy gap (E_g) values were calculated from the E_{ox} (onset) potential of electrochemical reduction and oxidation, which are charted in Table S1. The experimental HOMO-LUMO approximation was made with the support of cyclic voltammograms and the empirical relation for E_{HOMO} as [$(E_{ox}-E_{1/2}(\text{ferrocene})+4.8)$ eV. Ferrocene was used as standard. $E_{1/2}(\text{ferrocene})$ is equal to 0.304 V, which may be used to calculate the Energy of HOMO. We can calculate eV's bandgap (E_g) from the electronic absorption spectra $1242/\lambda$ (nm). Meanwhile, compounds **C1** and **C2** lead the HOMO, and their energy levels are comparable with minor variations. The value of the HOMO and LUMO and their energy gap of compounds are shown in Table 2. Whereas theoretical energy gap (ΔE) was calculated from TD-DFT approaches, the energy gap between HOMO and LUMO is 2.994 and 2.939 eV for complexes **C1** and **C2**, respectively. Therefore, it may determine the mode of interactions with other species within the molecule. Therefore, they are known as frontier orbitals. The HOMO mainly acts as an electron donor, while the LUMO orbital primarily accepts the electrons. The chemical stability of molecules is determined by the energy gap between HOMOs and LUMOs [39,40].

3.3. Thermogravimetric analysis.

This analysis deals with the studies of thermal stability, decomposition pattern, and structural features of a corresponding complex, $cis\text{-[RuCl}_2\text{(NO)(PPh}_3\text{)(L}_1\text{)]}$, which was recorded at a temperature range of 25-950°C. The TGA plot specified that the thermal

degradation proceeds in the four decomposition steps shown in Figure S6. The studied nitrosyl complexes are thermally stable at 240°C with minor weight loss, which indicates moisture removal. The first degradation step of C1 occurred in the range of 240-280°C, corresponding to the weight loss of one PPh₃ molecule. The weight loss is shown in the range of 280-310°C and is attributed to removing one NO molecule. The organic moieties of the Schiff base ligand are released in the third step, in the range of 360-480°C. The last degradation step is in the range of 480-540°C due to the loss of two chlorine molecules. The degradation steps over to the formation of solid residue or Ru₂O.

3.4. Molecular structural determinations.

The molecular structural evolutions of the studied nitrosyl complexes, namely **C1** and **C2**, were computed with DFT approaches. Figure 9 depicts a slightly distorted octahedron surrounding the geometry's Ru(II) center. The monobasic bidentate sulfa drug ligands contain O and N donor atoms in the basal plane. One Cl and one P atom, one remaining Cl NO group, are trans to each other and associated with the Ru center. The nitrosyl group is essentially linear and *trans*-positioned to be occupied by the Cl⁻, reliable with the NO stretching vibrations, indicating that the NO group is formally associated with the metal as NO⁺ [41]. The interatomic distance of N-O in both complexes **C1** and **C2** is (1.192 and 1.195 Å, respectively) and Ru-NO (1.763, Å) bond distance is shorter due to the π back bonding of the nitrosyl ligand. The interatomic distance of Ru-P (2.537 and 2.548 Å, for **C1** and **C2**, respectively). The computed Ru-N-O bond angle for **C1**, 174.75°, and **C2**, 177.47 are similar to other reported data [42]. The angle of atoms confirms the slight deviation of this octahedron in the trans site, which is diverse from 180° for the complexes described in Table 3. A sulfa drug Schiff base ligand binds with the ruthenium atom as monobasic bidentate ON donor atoms forming chelate of six-membered RuO₁₁C₆C₃C₂N₁₂ through a bite angle of O₍₁₁₎-Ru-N₍₁₂₎ 87.614.

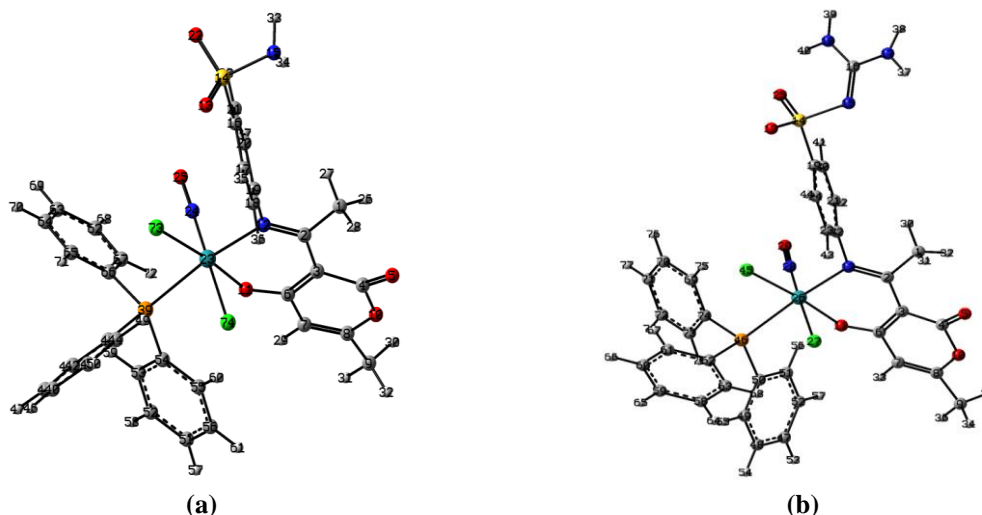


Figure 9. Optimized molecular structure for (a) **C1**; (b) **C2** with B3LYP and LANL2DZ.

Table 3. Geometrical parameters of *cis*-[RuCl₂(PPh₃)(NO)(L¹)] **C1** and *cis*-[RuCl₂(PPh₃)(NO)(L²)] **C2** (selected).

Bond connectivity	(Å)	Bond connectivity	(Å)
Ru-O(11)	2.046	Ru-O(11)	2.064
Ru-N(12)	2.124	Ru-N(12)	2.126
Ru-N(24)	1.762	Ru-Cl(27)	2.414
Ru-P(39)	2.537	Ru-N(28)	1.763
Ru-Cl(73)	2.480	Ru-Cl(45)	2.466

Ru-Cl(74)	2.429	Ru-P(46)	2.548
N(24)-O(25)	1.192	N(28)-O(29)	1.195
N(12)-C(2)	1.335	N(12)-C(2)	1.332
O(11)-C(6)	1.316	O(11)-C(6)	1.319
Bond connectivity	(°)	Bond connectivity	(°)
O(11)-Ru(23)-N(12)	88.092	O(11)-Ru(26)-N(12)	86.426
O(11)-Ru(23)-N(24)	94.771	O(11)-Ru(26)-Cl(27)	86.006
O(11)-Ru(23)-P(39)	88.837	O(11)-Ru(26)-N(28)	91.339
O(11)-Ru(23)-Cl(73)	174.515	O(11)-Ru(26)-Cl(45)	174.313
O(11)-Ru(23)-Cl(74)	87.731	O(11)-Ru(26)-P(46)	92.708
N(12)-Ru(23)-N(24)	94.099	N(12)-Ru(26)-Cl(27)	85.734
N(12)-Ru(23)-P(39)	172.344	N(12)-Ru(26)-N(28)	93.733
N(12)-Ru(23)-Cl(73)	96.994	N(12)-Ru(26)-Cl(45)	96.274
N(12)-Ru(23)-Cl(74)	84.705	N(12)-Ru(26)-P(46)	173.693
N(24)-Ru(23)-P(39)	93.144	Cl(27)-Ru(26)-N(28)	177.318
N(24)-Ru(23)-Cl(73)	86.936	Cl(27)-Ru(26)-Cl(45)	89.199
N(24)-Ru(23)-Cl(74)	177.195	Cl(27)-Ru(26)-P(46)	87.975
P(39)-Ru(23)-Cl(73)	85.862	N(28)-Ru(26)-Cl(45)	93.472
P(39)-Ru(23)-Cl(74)	88.167	N(28)-Ru(26)-P(46)	92.532
Cl(73)-Ru(23)-Cl(74)	90.688	Cl(45)-Ru(26)-P(46)	84.058
Ru(23)-N(24)-O(25)	174.748	Ru(26)-N(28)-O(29)	177.465

The two-chlorine atom is in a *cis* position to Cl₍₃₀₎-Ru-Cl₍₄₈₎, 90.936°, and the nitrosyl lie *trans* to chlorine. The interatomic distance of Ru-Cl (30) 2.425 Å is minor, while another chlorine atom presented in the same complexes, Ru-Cl (48) 2.484 Å, having some slight difference, is observed. This is expected due to the *trans*-strengthening effect of the NO group [43].

3.5. NLO properties.

NLO properties provide critical functions for optical materials like optical telecommunication, optical data storage, optical interconnects, integrated optical signal processing, and image reconstruction technologies of organic/inorganic materials and their potential applications. The dipole moment, molecular polarizability, and hyperpolarizability values should be higher to characterize the NLO activity of the molecules. Therefore, the NLO properties were theoretically calculated based on the relations of x, y, and z components [44,45] as given by the following equations (2 to 56). It is a tertiary tensor 3 × 3 × 3 matrices can describe. By using the following equation (6), Kleinman symmetry [46] allows for the condensing of the twenty-seven components of the 3D matrix to ten parts.

$$\mu = (\mu_x^2 + \mu_y^2 + \mu_z^2)^{1/2} \quad (2)$$

$$\alpha = 1/3(\alpha_{xx} + \alpha_{yy} + \alpha_{zz}) \quad (3)$$

$$\Delta\alpha = \left[\frac{(\alpha_{xx} - \alpha_{yy})^2 + (\alpha_{yy} - \alpha_{zz})^2 + (\alpha_{zz} - \alpha_{xx})^2}{2} \right]^{1/2} \quad (4)$$

$$(\beta_0) = (\beta_x^2 + \beta_y^2 + \beta_z^2)^{1/2} \quad (5)$$

and

$$\beta_x = \beta_{xxx} + \beta_{xyy} + \beta_{xzz} \quad (6)$$

$$\beta_y = \beta_{yyy} + \beta_{xxy} + \beta_{yzz} \quad (7)$$

$$\beta_z = \beta_{zzz} + \beta_{xxz} + \beta_{yyz} \quad (8)$$

or

$$(\beta_0) = [(\beta_{xxx} + \beta_{xyy} + \beta_{xzz})^2 + (\beta_{yyy} + \beta_{yzz} + \beta_{yxx})^2 + (\beta_{zzz} + \beta_{zxx} + \beta_{zyy})^2]^{1/2} \quad (9)$$

In connection with this, I calculated the NLO properties of all the studied nitrosyl complexes **C1** and **C2**. The computed values concerning their tensor orders are summarized in Table S2. The values in the order of dipole moment (μ), polarizability (α), anisotropy of the polarizability ($\Delta\alpha$) and hyperpolarizability (β) are 10.264D, -297.564×10^{-24} , 35.542×10^{-24} in au and 350.799×10^{-31} esu for complex **C1** and 8.373, -287.912×10^{-24} , 112.659×10^{-24} in au and 679.897×10^{-31} esu for complex **C2**, respectively. All the NLO properties are presented in the atomic units (au), and the calculated values have been converted into electrostatic units (esu) through the conversion factor of 0.148×10^{-24} esu for α and 8.639×10^{-33} esu for β and the only dipole moment unit is presented in D (debye). One of the model compounds used as NLO active material is urea[47]. Generally, highly efficient NLO materials are mainly consistent with noticeable charge transfer (CT) transitions. According to Figure 10, the extreme negative potential region is associated with the most electronegative atoms, while the top positive region is associated with the most electropositive atoms. In all the complexes, the sulfa drug moiety and chloride atoms' oxygen atoms bear more electronegative. At the same time, the leading positive region is localized on hydrogen atoms, which correspond to the neutral groups, and the remaining species are surrounded by a zero potential.

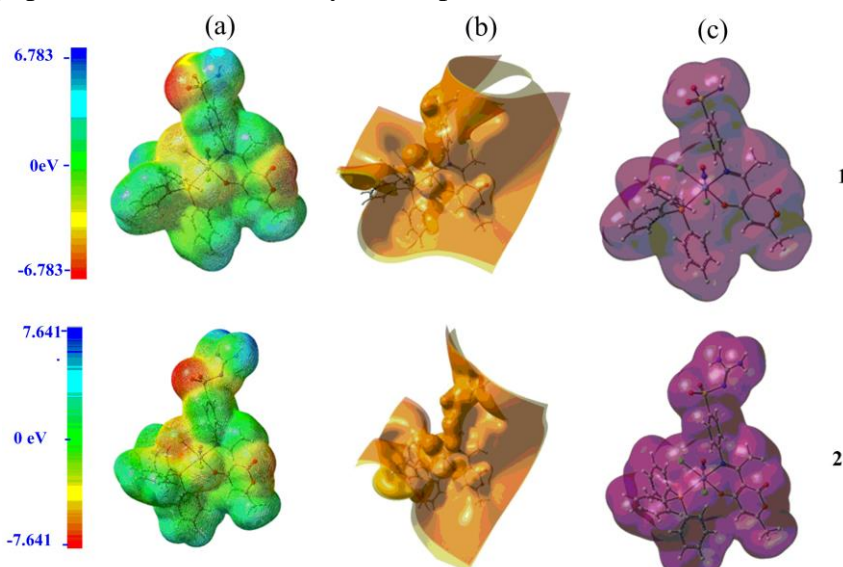


Figure 10. (a) MEPS; (b) ESP; (c) TED of the nitrosyl complexes **C1** and **C2**.

3.6. Antimicrobial activity.

The antibacterial evaluation of **C1** and **C2** has been screened against *E. coli*. The results are summarized in Table 4 and Figure S7. The results show that the Ru(II)-nitrosyl complexes in our investigation are more potent bactericides than the ligands. The chelation theory is one of the main criteria for the enhancement of the activity of complex compounds [48]. Chelation can reduce the metal ion's polarity and increase the chelate's lipophilicity, and the interaction between the metal ion and the lipid is favored. The lipophilicity of the complexes was discussed in ADME studies. Chelation is also considerable to reduce the metal ion polarization substantially due to the partial sharing of its positive charge with donor groups and possible π electron delocalization over the entire chelate ring. The lipids, as well as polysaccharides, are the main constituents of cell walls and membranes and are preferred for metal ion interactions. The breakdown of the cell's permeability barrier may interfere with normal cell processes. If the geometry and charge distribution around the molecule are incompatible with the geometry and charge distribution around the pores of the bacterial cell wall, penetration through the wall of

the toxic agent cannot occur. This poisonous reaction within the pores will be prevented. Chelation factor alone is not enough to determine the potency of antibacterial activity. Some significant factors such as the nature of the metal ion, the nature of the ligand, coordinating sites, size and shape of the molecules, concentration, hydrophilicity, lipophilicity, and presence of co-ligands have considerable influence on antibacterial activity. The potency of an antimicrobial agent is also determined by steric and pharmacokinetic factors. Lipophilic and polar substituents are expected to increase antibacterial activity. Metal complexes' antibacterial properties cannot be attributed solely to chelation but rather to a complex blend of various contributions.

Table 4. Average zone of Inhibition (mm±2) against *E. Coli* of compounds **C1** and **C2** at various concentrations in μM.

Complexes	100μM	50μM	25μM
C1	20	12	7
C2	18	12	8
Ampicillin	44	27	20
Solvent DMSO	0	0	0

3.7. Antioxidant activities.

In vitro, the antioxidant activity of the studied complex compounds **C1** and **C2** were evaluated through radical scavenging methods using DPPH• and NO•. The antioxidant property of the tested samples was evaluated at variable concentrations (20, 40, 60, 80, and 100 μg/mL), and butylated hydroxyl toluene (BHT) was used as a standard for the comparison of the activity. The IC₅₀ value of the studied complexes was calculated from the equation of the graph that you got ($Y = MX - C$), changed Y to 50 ($50 = MX - C$), and then made X the subject of the formula Figures S8 and S9. Therefore, the X value should correspond to your IC₅₀ value. The IC₅₀ value of the studied complexes was calculated from the equation of the graph that you got ($Y = MX - C$), changed Y to 50 ($50 = MX - C$), and then made X the subject of the formula Figures S8 and S9. Therefore, the X value should correspond to your IC₅₀ value. The IC₅₀ value of the studied compounds **C1** and **C2** in the DPPH• assay shows results [**C1**: 66.67 and **C2**: 57.95 (μM)]. While in the NO• assay shows results [**C1**: 81.18 and **C2**: 83.67 (μM)], which is charted in Table 5. Both compounds have good antioxidant activity in the assay described above. Thus, the lower the IC₅₀ value, the higher the antioxidant activity of the compounds [49]. The IC₅₀ value is a parameter widely used to measure the antioxidant activity of test samples [50].

Table 5. Inhibition (%) and of IC₅₀ antioxidant activity in DPPH assay for metal complexes **C1** and **C2**.

Conc. μM	C1		C2	
	DPPH	NO	DPPH	NO
20	34.14	25.40	35.43	27.04
40	41.93	38.04	40.24	36.75
60	54.25	45.22	49.14	45.50
80	59.63	50.40	54.45	51.65
100	64.02	52.07	60.12	53.33
IC ₅₀	66.67	81.18	57.95	83.67

3.8. In silico ADME studies.

In the present investigation, we move beyond these classical physicochemical properties (PC) to predict several absorption, distribution, metabolism, excretion, and toxicity (ADMET) parameters using online servers. These are displaying good biological potential and oral administrative actions. The ability to decide or predict potential drug candidates is now easier due to computational pharmacology and pharmacokinetic studies of drug-like properties [50]. Molecular hydrophobicity (log P), topological polar surface area (TPSA), and

bioavailability are all included in further information offered by the Swiss ADME predictor for the compounds. Five cytochrome phosphate (CYP) models, including (CYP1A2, CYP2C19, CYP2C9, CYP2D6, and CYP3A4) inhibitors, and one phosphatase glycoprotein (P-GP) substrate, are used to predict metabolism. These parameters were computed and verified to be within their standard ranges. In Table S4, the *in silico* ADME properties of the synthetic ligands and their complexes are shown. Figure S10 presents the Egg model, which combines cheminformatics and physicochemical properties of ligand complexes **C1** and **C2**. The topological polar surface area is one of the prominent physicochemical parameters to be analyzed by hydrogen bonds. The power of this system is used to predict drug transport action inside the various body parts like the gastrointestinal tract and penetration of the blood-brain barrier (BBB). In the molecule, there are several hydrogen bond donors (HBD) and hydrogen bond acceptors (HBA). Nine rotatable bonds make up the compound, which makes it suitable for oral administration. Observations of our studied compounds which meet only the two criteria of (i) rotatable bonds (10 or less) and (ii) polar surface area equal to or less than 140 Å² (or 12 or less H-bond donors and acceptors) will have a high probability of good oral bioavailability in the rat. Molecules that have a polar surface area of more than 140 Å² tend to have a difficult time passing through cell membranes. In addition, if the bioactive score exceeds zero, it is more likely that the substance being examined has enhanced biological activity. The molecule's potency and many ADME parameters are determined by lipophilicity, which is characterized by computed log P values. Lipinski's rule suggests that log P values of less than five are indicative of a greater tendency to facilitate penetration into the cell membrane. All tested compounds had log P values less than 5, and all ligands and complexes have a greater tendency to penetrate the cell membrane. At the same time, complex **C1** has a higher tendency to penetrate the cell membrane. The solubility score (log S) defines the soluble behavior of the compound. It is defined in the order of < -10; insoluble, < -6; poorly soluble, < -4; moderate soluble, < -2; soluble, and < 0; highly soluble. In the current study, the log S score of the ligand's molecules is mostly around -4.0, so these are moderately soluble. The log S values in this study of the ligand's molecules are between -2.38 and -2.56, representing moderate solubility in the water. In comparison, the complexes are poorly soluble in water because the log S values are -8.4 to -9.0.

4. Conclusions

In this manuscript, we have reported the design, synthesis, experimental-theoretical spectral properties, and computed molecular structure of Ru-NO complexes cis-[RuCl₂(NO)(PPh₃)(L_{1,2})]. The vibrational intensities, electronic absorption intensity, and ¹HNMR spectra were computed and correlated with experimental data. ¹HNMR and vibrational spectra were computed and compared with experimental data observed in a similar way. The thermal stability of the compounds was confirmed by TGA analysis. Similarly, the antioxidant and antimicrobial activity of the studied complexes were investigated. The complexes were more potent against *E. coli*, having a zone of inhibitions ~18 in 100µM. Also, the complexes were excellent oxidizing agents, having IC₅₀= 66.67 and 57.95 µM in DPPH• and 81.18 and 83.67 µM NO• assay values. The FMOs analyses and some chemical properties depending on them and NLO properties, atomic charges, NBOs, and surface analyses like ESP, TED, and MESP were theoretically investigated for both complex compounds. The total dipole moment, polarizability, and hyperpolarizability of the title compounds were also calculated. The ADME results from *in silico* can be traced back to good pharmacokinetics and biological

activity. The bioavailability score and TPSA value of studied compounds are ~0.55 and 131.34-196.10 Å², respectively.

Funding

This research received no external funding.

Acknowledgments

The authors highly acknowledge our Vice-Chancellor, Professor Rajesh Kumar Verma, for their blessing, support, and motivation. We are also thankful to our department for encouraging and providing instrumental facilities. In addition, analytical facilities provided by the Central Drug Research Institute, Lucknow, are gratefully acknowledged.

Conflicts of Interest

The authors declare no conflict of interest.

References

1. Tfouni, E.; Truzzi, D.R.; Tavares, A.; Gomes, A.J.; Figueiredo, L.E.; Franco, D.W. Biological activity of ruthenium nitrosyl complexes. *Nitric Oxide* **2012**, *26*, 38-53, <https://doi.org/10.1016/j.niox.2011.11.005>.
2. Stepanenko, I.; Zalibera, M.; Schaniel, D.; Telser, J.; Arion V. B. Ruthenium-nitrosyl complexes as NO-releasing molecules, potential anticancer drugs, and photoswitches based on linkage isomerism. *Dalton Trans* **2022**, *51*, 5367-5393, <https://doi.org/10.1039/D2DT00290F>.
3. Xiang, H.J.; Guo, M.; Liu, J.G. Transition-Metal Nitrosyls for Photocontrolled Nitric Oxide Delivery. *European Journal Inorganic Chemistry* **2017**, 1586-1595, <https://doi.org/10.1002/ejic.201601135>.
4. Heinrich, T.A.; Da Silva, R.S.; Miranda, K.M.; Switzer, C.H.; Wink, D.A.; Fukuto, J. M. Biological nitric oxide signalling: chemistry and terminology. *British Journal of Pharmacology* **2013**, *169*, 1417-1429, <https://doi.org/10.1111/bph.12217>.
5. Astuti, R.I.; Nasuno, R.; Takagi, H. Nitric Oxide Signalling in Yeast. *Advanced Microbiology Physiology* **2018**, *72*, 29-63, <https://doi.org/10.1016/bs.ampbs.2018.01.003>.
6. Che, X.; Fang, Y.; Si, X.; Wang, J.; Hu, X.; Reis, C.; Chen, S. The Role of Gaseous Molecules in Traumatic Brain Injury: An Updated Review. *Frontier Neuroscience* **2018**, <https://doi.org/10.3389/fnins.2018.00392>.
7. Wu, Y.; Ding, Y.; Ramprasath, T.; Zou, Ming-Hui. Oxidative Stress, GTPCH1, and Endothelial Nitric Oxide Synthase Uncoupling in Hypertension. *Antioxidants & Redox Signaling* **2021**, 750-764, <http://doi.org/10.1089/ars.2020.8112>.
8. Ritchie, R.H.; Drummond, G.R.; Sobey, C.G.; De Silva, T.M.; Kemp-Harper, B.K. The opposing roles of NO and oxidative stress in cardiovascular disease. *Pharmacology Research* **2017**, *116*, 57-69, <https://doi.org/10.1016/j.phrs.2016.12.017>.
9. Crisalli, M.A.; Franco, L.P.; Silva, B.R.; Holanda, A.K.M.; Bendhack, L.M.; Da Silva, R.S.; Ford, P.C. Nitric oxide release from a photoactive water-soluble ruthenium nitrosyl. Biological effects. *Journal of Coordination Chemistry* **2018**, *71*, 1690-1703, <https://doi.org/10.1080/00958972.2018.1469129>.
10. Patra, A.K.; Mascharak, P.K. A Ruthenium Nitrosyl That Rapidly Delivers NO to Proteins in Aqueous Solution upon Short Exposure to UV Light. *Inorganic Chemistry* **2003**, *42*, 7363-7365, <https://doi.org/10.1021/ic030110h>.
11. Ferrarini, A.; Soek, R.N.; Rios, R.R.; Santana, F.S.; Campos, R.B.; da Silva, R.S.; Nunes, F.S. Structural, spectral, and photoreactivity properties of mono and polymetallated-2,2'-bipyridine ruthenium(II) complexes. *Inorganica Chimica Acta* **2022**, *533*, 120771, <https://doi.org/10.1016/j.ica.2021.120771>.
12. Kumar, S.; Singh, S.; Ghosh, K. Ruthenium Nitrosyl Complexes: Photoinduced Delivery of NO to Different Biological Targets. In: Ray, A.; Gulati, K. *Nitric Oxide: From Research to Therapeutics. Advances in Biochemistry in Health and Disease, Springer, Cham.* **2023**, *22*, https://doi.org/10.1007/978-3-031-24778-1_21.

13. Elnaggar, M.A.; Subbiah, R.; Han, D.K.; Joung, Y.K. Lipid-based carriers for controlled delivery of nitric oxide. *Expert Opinion Drug Delivery* **2007**, *14*, 1341-1353, <https://doi.org/10.1080/17425247.2017.1285904>.
14. Xu, L.; Ma, Z.; Wang, W.; Xie, L.; Liu, L.; Liu, J.; Zhao, X.; Wang, H. Photoinduced cytotoxicity, photo-controlled nitric oxide release and DNA/human serum albumin binding of three water-soluble nitrosylruthenium complexes. *Polyhedron* **2017**, *137*, 157-164, <https://doi.org/10.1016/j.poly.2017.08.036>.
15. Wu, F.; Wang, C.J.; Lin, H.; Jia, A.Q.; Zhang, O.F. Syntheses, structures and catalytic properties of ruthenium(II) nitrosyl complexes with bidentate and tetradentate Schiff base ligands. *Inorganica Chimica Acta* **2018**, *471*, 718-723, <https://doi.org/10.1016/j.ica.2017.12.004>.
16. Kostin, G.A.; Kozlov, R.; Bogomyakov, A.; Tolstikov, S.; Sheven, D.; Korenev, S. New Ruthenium Nitrosyl Complexes Combining Potentially Photoactive Nitrosyl Group with the Magnetic Nitroxide Radicals as Ligands. *International Journal of Molecular Sciences* **2023**, *17*, 13371, <https://doi.org/10.3390/2Fijms241713371>.
17. Talotta, F.; Heully, J.L.; Alary, F.; Dixon, I.M.; Gonzalez, L.; Boggio-Pasqua, M. Linkage Photoisomerization Mechanism in a Photochromic Ruthenium Nitrosyl Complex: New Insights from an MS-CASPT2 Study. *Journal of Chemistry Theory Computation* **2017**, *13*, 6120-6130, <https://doi.org/10.1021/acs.jctc.7b00982>.
18. Abucayon, E.G.; Powell, D.R.; Richter-Addo, G.B. Carbon-Nitrogen and Nitrogen-Nitrogen Bond Formation from Nucleophilic Attack at Coordinated Nitrosyls in Fe and Ru Heme Models. *Journal of American Chemical Society* **2017**, *139*, 9495-9498, <https://doi.org/10.1021/jacs.7b05209>.
19. Yamaletdinov, R.D.; Zilberberg, I.L. The Effect of *trans* Ligands in the NO-Linkage Reverse Isomerization for Ruthenium-Nitrosyl-Tetraammine Complexes: A DFT Study. *European Journal of Inorganic Chemistry* **2017**, 2951-2954, <https://doi.org/10.1002/ejic.201700138>.
20. Awasabisah, D.; Xu, N.; Gautam, K.P.S.; Powell, D.R.; Shaw, M.J.; Richter-Addo, G. B. Preparation, Characterization, Electrochemistry, and Infrared Spectro electrochemistry of Ruthenium Nitrosyl Porphyrins Containing η^1 -O-Bonded Axial Carboxylates. *European Journal of Inorganic Chemistry* **2016**, *2016*, 509-518, <https://doi.org/10.1002/ejic.201501115>.
21. Novak, M.S.; Büchel, G.E.; Keppler, B.K.; Jakupec, M.A. Biological properties of novel ruthenium- and osmium-nitrosyl complexes with azole heterocycles. *Journal of Biological Inorganic Chemistry* **2016**, *21*, 347-356, <https://doi.org/10.1007/s00775-016-1345-z>.
22. Detty, M.R.; Gibson, S.L.; Wagner, S.J. Current clinical and preclinical photosensitizers for use in photodynamic therapy. *Journal of Medicinal Chemistry* **2004**, *47*, 3897-3915, <https://doi.org/10.1021/jm040074b>.
23. Wu, B.; Ong, M.S.; Groessl, M.; Adhireksan, Z.; Hartinger, C.G.; Dyson, P.J.; Davey, C.A. A ruthenium antimetastasis agent forms specific histone protein adducts in the nucleosome core. *Chemistry European Journal* **2011**, *17*, 3562-3566, <https://doi.org/10.1002/chem.201100298>.
24. Adhireksan, Z.; Davey, G.E.; Campomanes, P.; Groessl, M.; Clavel, C.M.; Yu, H.; Nazarov, A.A.; Yeo, C.H.F.; Ang, W.H.; Droge, P.; Rothlisberger, U.; Dyson, P.J.; Davey, C.A. Ligand substitutions between ruthenium-cymene compounds can control protein versus DNA targeting and anticancer activity. *Natural Communication* **2014**, *5*, 1-13, <https://doi.org/10.1038/ncomms4462>.
25. Silva, R.S.; de Lima, R.G.; Machado, S.P. Design, Reactivity, and Biological Activity of Ruthenium Nitrosyl Complexes. *Advanced Inorganic Chemistry* **2015**, *67*, 265-294, <https://doi.org/10.1016/bs.adioch.2014.11.001>.
26. Mir, J.M.; Maurya, R.C. Synthesis and DFT supported spectroscopic characterization of a pyrazolone Schiff base complex of Ru^{II}-NO core, *Inorganic and Nano-Metal Chemistry* **2023**, *53*, 570-578, <https://doi.org/10.1080/24701556.2023.2165679>.
27. Amani, F. H. N.; Safa, W.A.; Samia, A. S.; Magdy, M. M.; Yasmin, M. A.; Ramadan, M.R.; Mostafa, M.E. Molecular Design, Spectroscopic, DFT, Pharmacological, and Molecular Docking Studies of Novel Ruthenium(III)-Schiff Base Complex: An Inhibitor of Progression in HepG2 Cells. *International Journal of Environmental Research and Public Health* **2022**, *19*, 13624, <https://doi.org/10.3390/ijerph192013624>.
28. Li, T.; Li, S.; Dong, Y.; Zhu, R.; Liu, Y. Antioxidant activity of penta-oligogalacturonide, isolated from haw pectin, suppresses triglyceride synthesis in mice fed with a high-fat diet. *Food Chemistry* **2014**, *145*, 335-341, <https://doi.org/10.1016/j.foodchem.2013.08.036>.

29. Green, L.C.; Wagner, D.A.; Glogowski, J.; Skipper, P.L.; Wishnok, J.K.S.R. Analysis of nitrate, nitrite, and [15N]nitrate in biological fluids. *Analytical Biochemistry* **1982**, *126*, 131-138, [https://doi.org/10.1016/0003-2697\(82\)90118-x](https://doi.org/10.1016/0003-2697(82)90118-x).
30. Marcocci, L.; Maguire, J.J.; Droy-Lefaix, M.T.; Packer, L. The nitric oxide-scavenging properties of Ginkgo biloba extract EGb 761. *Biochemical Biophysics Research Communication* **1994**, *201*, 748-755, <https://doi.org/10.1006/bbrc.1994.1764>.
31. Frisch, M. J.; Trucks, G.W.; Schlegel, H.B.; Scuseria, G.E.; Robb, M.A.; Cheeseman, J.R.; Zakrzewski, V.G.; Montgomery, Jr, J.A.; Stratmann, R.E.; Burant, J.C.; Dapprich, S.; Millam, J.M.; Daniels, A.D.; Kudin, K.N.; Strain, M.C.; Farkas, O.; Tomasi, J.; Barone, V.; Cossi, M.; Cammi, R.; Mennucci, B.; Pomelli, C.; Adamo, C.; Clifford, S.; Ochterski, J.; Petersson, G.A.; Ayala, P.Y.; Cui, Q.; Morokuma, K.; Reg, N.; Salvador, P.; Dannenberg, J.J.; Malick, D.K.; Rabuck, A.D.; Rahavachari, K.; Foresman, J.B.; Cioslowski, J.; Ortiz, J.V.; Baboul, A.G.; Stefanov, B.B.; Liu, G.; Liashenko, A.; Komaromi, P.P.; Gomperts, R.; Martin, R.L.; Fox, D.; Keith, T.; AlLaham, M.A.; Peng, C.Y.; Nanayakkara, A.; Challa Combe, M.; Gill, P.; Johnson, B.; Chen, W.; Wong, M.W.; Andres, J.L.; Gonzalez, Head Gordon, M.; Replogle, E.S.; Pople, J.A. Gaussian09, Revision A11.4, Gaussian Inc Pittsburgh **2010**.
32. Dennington, R.; Keith, T.; Millam, J. Gauss View, Version 5, Semicem Inc., Shawnee Mission KS **2009**.
33. Casida, M.E. Time-Dependent Density Functional Response Theory of Molecular Systems: Theory, Computational Methods, and Functionals. In *Theoretical and Computational Chemistry, Seminario, J.M., Ed.; Elsevier: 1996; Volume 4*, pp. 391-439, [https://doi.org/10.1016/S1380-7323\(96\)80093-8](https://doi.org/10.1016/S1380-7323(96)80093-8).
34. Bottomley, F.; White, P.S.; Mukaida, M.; Shimura, K.; Kakihana, H. Electrophilic behaviour of nitrosyls: the reactions of ketones with nitrosyls and the crystal and molecular structure of the product of the reaction between *trans*-chloro(nitrosyl)tetra(pyridine)ruthenium and acetone. *J. Chem. Soc. Dalton Trans.* **1988**, 2965-2969, <https://doi.org/10.1039/DT9880002965>.
35. Kim, M.; Park, S.; Song, D.; Moon, D.; You, Y.; Lim, M.; Lee, H.-I. Visible-light NO photolysis of ruthenium nitrosyl complexes with N₂O₂ ligands bearing π -extended rings and their photorelease dynamics. *Dalton Transactions* **2022**, *51*, 11404-11415, <https://doi.org/10.1039/D2DT01019D>.
36. Mir, J.M.; Jain, N.; Jaget, P.S.; Khan, W.; Vishwakarma, P.K.; Rajak, D.K.; Malik, B. A.; Maurya, R.C. Urinary tract anti-infectious potential of DFT-experimental composite analyzed ruthenium nitrosyl complex of N-dehydroacetic acid-thiosemicarbazide. *Journal of King Saud University-Science* **2019**, *31*, 89-100, <https://doi.org/10.1016/j.jksus.2017.06.006>.
37. Golfeto, C.C.; Poelhsitz, G.V.; Selistre-de-Araújo, H.S.; deAraujo, M.P.; Ellena, J.; Castellano, E.E.; Lopes, L.G.L.; Moreira, I.S.; Batista, A.A. Synthesis, characterization and cytotoxic activities of the [RuCl₂(NO)(dppp)(L)]PF₆ complexes. *Journal of Inorganic Biochemistry* **2010**, *104*, 489-495, <https://doi.org/10.1016/j.jinorgbio.2009.12.015>.
38. Kumar, S.A.; Bhaskar, B.L. Structural elucidation of antihemorrhage drug molecule Diethylammonium 2,5-dihydroxybenzene sulfonate - an *insilico* approach. *IOP Conf. Ser.: Material Science Engineering* **2018**, *310*, 012124, <https://doi.org/10.1088/1757-899X/310/1/012124>.
39. Parte, M.K.; Vishwakarma, P.K.; Jaget, P.S.; Maurya, R.C. Synthesis, spectral, FMOs and NLO properties based on DFT calculations of dioxidomolybdenum(VI) complex. *Journal of Coordination Chemistry* **2021**, *74*, 584-597, <https://doi.org/10.1080/00958972.2021.1880574>.
40. Sagir, M.; Mushtaq, K.; Khalid, M.; Khan, M.; Tahir, M.B.; Braga, A.A.C. Exploration of linear and third-order nonlinear optical properties for donor- π -linker-acceptor chromophores derived from ATT-2 based non-fullerene molecule. *RSC Advance* **2023**, *1*, 31855-31872, <https://doi.org/10.1039/D3RA04580C>.
41. G.B. Richter-Addo, P. Legzdins, *Metal Nitrosyl*, Oxford University Press: New York **1992**.
42. Liu, C.; Wang, Y.; Wang, A.; Su, F.; Wang, H. Structures, spectral and photodynamic properties of two nitrosylruthenium (II) isomer complexes containing 8-quinolinolate and L-proline ligands. *Results in Chemistry* **2022**, *4*, 100318, <https://doi.org/10.1016/j.rechem.2022.100318>.
43. Haymore, B.L.; Ibers, J.A. Comparison of linear nitrosyl and singly bent aryldiazo complexes of ruthenium. Structures of trichloronitrosylbis(triphenylphosphine)ruthenium, RuCl₃(NO)(P(C₆H₅)₃)₂, and trichloro(p-tolyl)diazobis(triphenylphosphine)ruthenium-dichloromethane, RuCl₃(p-NNC₆H₄CH₃)(P(C₆H₅)₃)₂.CH₂Cl₂. *Inorganic Chemistry*, **1975**, *14*, 3060-3070, <https://doi.org/10.1021/ic50154a041>.
44. Maurya, R.C.; Malik, B.A.; Mir, J.M.; Vishwakarma, P.K. Oxidovanadium(IV) complexes involving dehydroacetic acid and β -diketones of bioinorganic and medicinal relevance: Their synthesis,

- characterization, thermal behavior and DFT aspects. *Journal of Molecular Structure* **2015**, *1083*, 343-356, <https://doi.org/10.1016/j.molstruc.2014.11.032>.
45. Khan, M.U.; Hussain, S.; Asghar, M.A.; Munawar, K.S.; Khera, R.A.; Imran, M.; Ibrahim, M.M.; Hessien, M.M.; Mersal, G.A.M. Exploration of Nonlinear Optical Properties for the First Theoretical Framework of Non-Fullerene DTS(FBTTh₂)₂-Based Derivatives. *ACS Omega* **2022**, *7*, 18027-18040, <https://doi.org/10.1021/acsomega.2c01474>.
 46. Kleinman, D.A. Nonlinear Dielectric Polarization in Optical Media. *Physical Review* **1962**, *126*, 1977-179, <https://doi.org/10.1103/PhysRev.126.1977>.
 47. Mishma, J.N.C.; Jothy, V.B; Narayana, B.; Kodlady, S.N.; Alharbi, N.S. Abbas, G. Muthu, S. Synthesis, DFT, solvent effect and biological attributes of NLO active 4-bromo-2-((2-(2,4-Dinitrophenyl) hydrazono)methyl) phenol -Potent drug anti-brain cancer. *Journal of Molecular Structure* **2023**, *1289*, 135839, <https://doi.org/10.1016/j.molstruc.2023.135839>.
 48. Heyd, J.; Scuseria, G.E. Assessment and validation of a screened Coulomb hybrid density functional. *Journal of Chemical Physics* **2004**, *120*, 7274-7280, <https://doi.org/10.1063/1.1668634>.
 49. Thimmaiah, K.N.; Lloyd W.D.; Chandrappa, G.T. Stereochemistry and fungitoxicity of complexes of *p*-anisaldehydethiosemicarbazone with Mn(II), Fe(II), Co(II) and Ni(II). *Inorganica Chimica Acta* **1985**, *106*, 81-83, [https://doi.org/10.1016/S0020-1693\(00\)82252-5](https://doi.org/10.1016/S0020-1693(00)82252-5).
 50. Akullo, J.O.; Kiage-Mokua, B.N.; Nakimbugwe, D.; Ng'ang'a, J.; Kinyuru, J. Phytochemical profile and antioxidant activity of various solvent extracts of two varieties of ginger and garlic. *Heliyon* **2023**, *9*, e18806, <https://doi.org/10.1016/j.heliyon.2023.e18806>.
 51. Ahmad, I.; Kuznetsov, A.E.; Pirzada, A.S.; Alsharif, F.A.; Daglia, M.; Khan, H. Computational pharmacology and computational chemistry of 4-hydroxyisoleucine: Physicochemical, pharmacokinetic, and DFT-based approaches. *Frontiers in Chemistry* **2023**, *11*, <https://doi.org/10.3389/fchem.2023.1145974>.

Supplementary materials

Table S1. Electrochemical properties of **C1** and **C2** complexes.

Comp.	Scan rate mV/s	E_{pc1} (V)	I_{pc1} (A)	E_{pc2} (V)	I_{pc2} (μ A)	E_{pa2} (V)	I_{pa1} (μ A)	E_r (V)	ΔE (V)	I_{pa}/I_{pc}
C1	100	0.179	-0.893	-0.581	-2.752	-0.223	0.583	-0.402	0.358	0.212
	200	0.077	-1.330	-0.705	-4.683	-0.135	1.567	-0.420	0.570	0.335
	300	0.080	-1.676	-0.783	-6.087	-0.077	2.442	-0.430	0.860	0.401
	500	0.086	-2.023	-0.832	-6.980	-0.035	3.044	-0.434	0.797	0.436
C2	100	0.168	-0.353	-0.639	-3.624	-0.190	0.959	-0.415	0.449	0.265
	200	0.105	-0.245	-0.780	-5.784	-0.088	2.038	-0.434	0.692	0.352
	300	0.096	-1.535	-0.835	-6.687	-0.030	2.810	-0.433	0.805	0.420
	500	0.085	-1.989	-0.930	-8.472	-0.039	3.890	-0.485	0.891	0.459

Table S2. NLO properties (μ), (α), ($\Delta\alpha$) and (β) for complexes **C1** and **C2**.

	C1	C2
μ_x	-8.884	3.934
μ_y	2.408	1.877
μ_z	4.543	-7.149
$\mu_{Tot.}$	10.264	8.373
α_{xx}	-277.324	-213.282
α_{yy}	-318.353	-332.538
α_{zz}	-297.014	-317.916
α_{xy}	24.410	-26.884
α_{xz}	-4.147	18.835
α_{yz}	8.131	-7.901
α	-297.564×10^{-24}	-287.912×10^{-24}
$\Delta\alpha$	35.542×10^{-24}	112.659×10^{-24}
β_{xxx}	-15.459	-832.242
β_{yyy}	-129.707	-142.671
β_{zzz}	37.651	33.787
β_{xyy}	-281.204	181.258
β_{xxy}	283.706	314.311
β_{xxz}	19.271	-221.716
β_{xzz}	-18.221	56.762
β_{yzz}	-43.409	-35.884
β_{yyz}	50.163	-113.286
β_{xyz}	7.470	-62.984
$\beta(0)$	350.799×10^{-31}	679.897×10^{-31}

Table S3. Quantum chemical parameters of complexes **C1** and **C2** the values are given in eV.

Parameters	C1	C2
H	-6.640	-6.395
H-1	-6.803	-6.613
H-2	-6.939	-6.749
L	-3.646	-3.456
L+1	-3.619	-3.429
L+2	-2.395	-2.313
$\Delta E_{(H-L)}$	2.994	2.939
$\Delta E_{(H-1-L+1)}$	3.184	3.184
$\Delta E_{(H-2-L+2)}$	4.544	4.436
η	1.497	1.470
χ	5.143	4.926
μ	-5.143	-4.926

S	0.334	0.340
ω	8.834	8.254

Table S4. Insilco ADME properties of the ligands and complexes.

Parameters	HL ¹	HL ²	C1	C2
MW(g/mol)	322.34	364.38	785.60	827.64
heavy atoms	22	25	46	49
Aromatic heavy atoms	12	12	30	30
Fraction Csp ³	0.14	0.13	0.06	0.06
Rotatable bonds	3	4	6	7
H-bond acceptors	7	7	8	8
H-bond donors	2	3	1	2
Molar Refractivity	81.46	92.66	182.66	193.86
TPSA (Å ²)	131.34	169.72	157.72	196.10
Log P	1.30	0.84	3.58	3.35
LogS	-2.56	-2.38	-9.00	-8.84
GI absorption	High	Low	Low	Low
BBB permeant	No	No	No	No
P-gp substrate	No	No	No	No
CYP1A2	No	No	Yes	Yes
CYP2C19	No	No	No	No
CYP2C9	No	No	No	No
CYP2D6	No	No	No	No
CYP3A4	No	No	Yes	No
Log K _p cm/s	-7.68	-8.31	-6.36	-6.97
Bioavailability	0.55	0.55	0.55	0.17
Synthetic accessibility	3.40	3.68	6.08	6.30

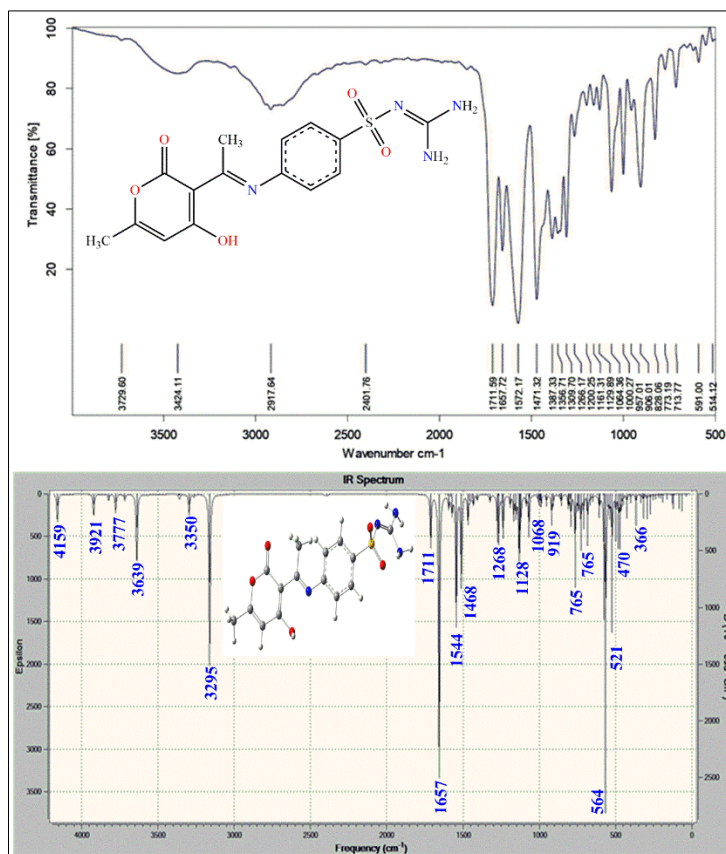


Figure S1. Experimental (a) and theoretical (b) IR spectrum of HL².

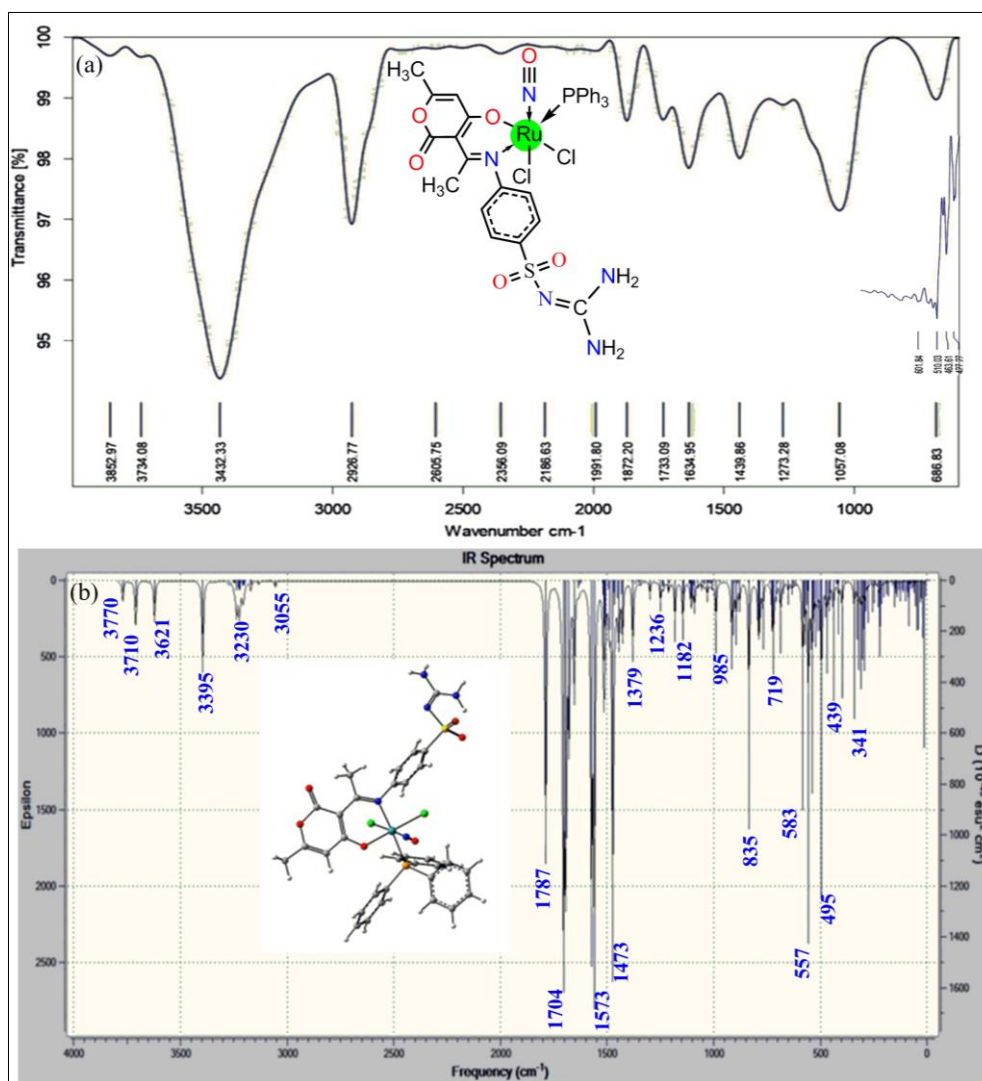


Figure S2. IR spectrum of *cis*-[RuCl₂(NO)(PPh₃)(L²)] C2 experimental (a) and theoretical (b).

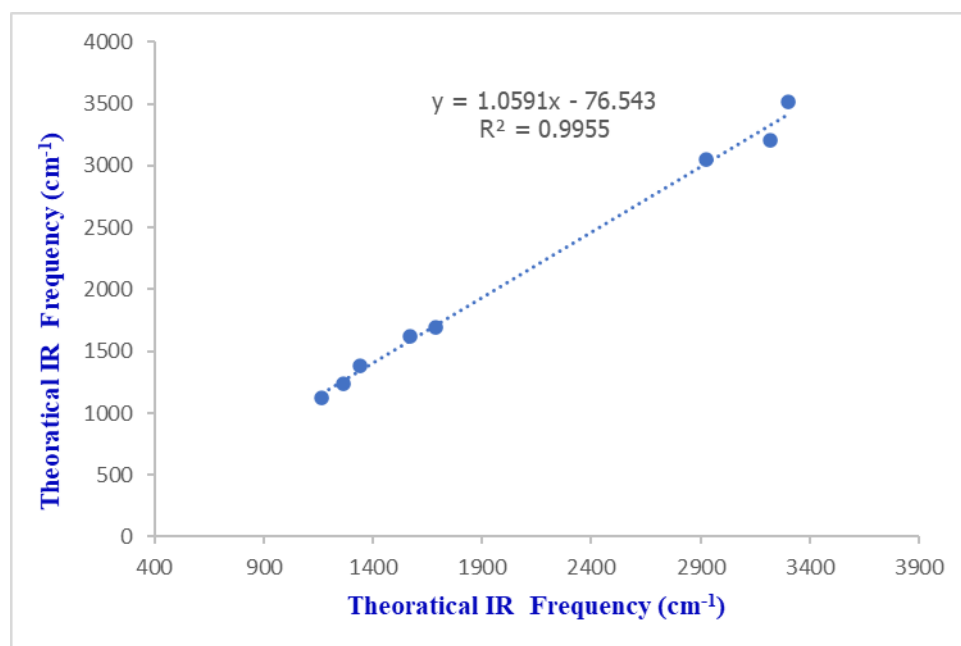


Figure S3. The relationship graphs between the experimental and theoretical vibrational frequency of HL¹.

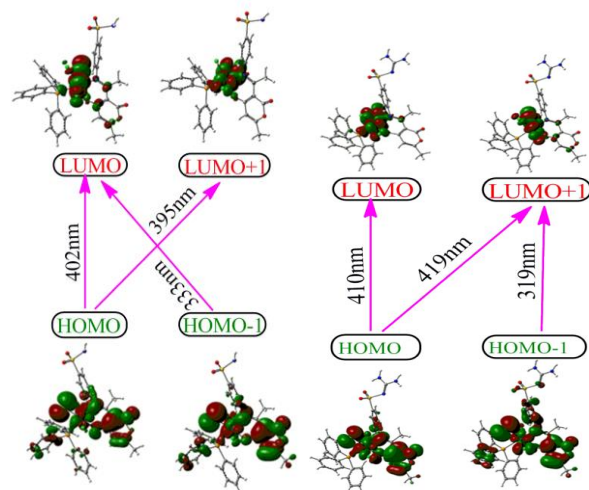


Figure S4. FMOs involved in electronic transition observed in TD-DFT computed UV-Vis. spectra of **C1** and **C2**.